Electro-chemo-mechanical analysis of a solid oxide cell based on doped ceria

C. Lenser,[1,*] J. Zhang,[2] N. Russner,[3] A. Weber,[3] O. Guillon[1,4,5] and N.H. Menzler[1]

1: Institute of Energy and Climate Research – Materials Synthesis and Processing (IEK-1), Forschungszentrum Jülich GmbH, Jülich, Germany

2: Department of Energy Conversion and Storage, Technical University of Denmark, DK-2800 Kgs. Lyngby, Denmark

3: Institute for Applied Materials – Electrochemical Technologies (IAM-ET), Karlsruhe Institute of Technology, Karlsruhe, Germany

4: Department of Ceramics and Refractory Materials, Institute of Mineral Engineering, RWTH Aachen University, Aachen, Germany

5: JARA-ENERGY, Jülich Aachen Research Alliance, Jülich, Germany

Abstract

Doped ceria has been investigated as an electrolyte material for solid oxide cells (SOC) for several decades due to its high ionic conductivity. However, ceria is reduced under fuel conditions in SOCs and becomes a mixed ionic-electronic conductor (MIEC). One of the issues arising is the chemical expansion of the electrolyte, which is a function of the oxygen activity μO_2 inside the electrolyte and therefore inhomogeneous across the electrolyte thickness. A one-dimensional model that enables the calculation of elastic stresses in the cell on the basis of the cell geometry and materials properties is developed for both fuel cell and electrolysis operation. Ceria is subjected to a decreased oxygen activity at the interface to the fuel electrode during electrolysis operation, leading to substantial mechanical stresses in the electrolyte

layers. Cell failure is observed under high electrolysis currents for a high-performance cell based on a doped-ceria electrolyte. We model the electro-chemo-mechanically-induced elastic stresses in the multilayer system of the cell and show that it peaks for operation at 750 °C and high current densities, in agreement with the observed onset of cell failure. Furthermore, the influence of the cell constraints on the elastic stresses is discussed for four different constraint cases.

1. Introduction

The reduction of CO_2 emissions across all energy sectors will require robust coupling between different energy sectors, such as electricity and transportation, in order to fully decarbonize the energy system. Fuel and electrolysis cells are key technologies for sector-coupling that turn chemical fuel into electrical energy and electrical energy into chemical fuel, respectively. Solid oxide cells (SOC) operate at high temperatures (typically 600 – 850 °C) and therefore are particularly attractive as electrolyzer cells (SOEC), with demonstrated system efficiencies > 80%.[1] SOCs can also be operated reversibly, generating electricity from fuels and vice versa in the same system with very high efficiency.[2]

The state-of-the-art SOEC utilize an electrolyte made from stabilized zirconia due to the materials excellent stability, while there is a trend to replace the conventional Ni-zirconia cermet fuel electrodes by electrodes based on Ni and doped ceria (often doped with Gadolinium, GDC, or Samarium, SDC) for metal- and electrolyte-supported cell designs.[3] For fuel electrode supported cells (FESC), however, the co-sintering of the half cell (support, electrode and electrolyte) at high temperatures creates unwanted interdiffusion between the zirconia electrolyte and the ceria electrode, resulting in the formation of low conductivity phases and porosity at the interface, resulting in poor performance.[4]

One possible solution is the utilization of doped ceria as the electrolyte to avoid unwanted interdiffusion during the high-temperature sintering step. However, doped ceria is partially reduced under SOEC fuel conditions, introducing a number of problems for SOEC operation:

i) the chemical reduction introduces electronic conductivity in the electrolyte, which critically reduces efficiency as large parts of the applied current density in the electrolysis cell are electronic and not ionic. Such parasitic currents make the cell resistance appear extremely small while hydrogen production is almost negligible.

ii) the formation of oxygen vacancies induces a lattice expansion in the material known as chemical expansion.[5] This leads to mechanical stresses in the cell and can result in cell failure.

Prior work on the stresses induced through the chemical expansion of ceria as an electrolyte in solid oxide fuel / electrolysis cells (SOFC / SOEC) have concluded that a safe use of a doped ceria electrolyte is limited to a certain maximum temperature. [6-8] Whereas Atkinson concentrated on the use of doped ceria in SOFCs,[6] Zhu investigated the use of ceria in SOECs,[7] concluding that SOECs containing a ceria electrolyte should not be operated above 700 °C (better 600 °C) to avoid critical tensile stresses at the interface to the air electrode. Both Zhu and Atkinson consider electrolyte-supported cells. Kim et al. observed that a thin, supported Nd-doped ceria electrolyte was more prone to electro-chemo-mechanical damage under changing operation conditions.[9] However, an explicit treatment of the stresses in a supported ceria electrolyte under different operation conditions is missing.

This paper examines the electro-chemo-mechanical stresses arising in a thin (3.5 μm) GDC electrolyte supported by a thick (450 μm) Ni-YSZ support under different operation conditions in fuel cell and electrolysis operation. A cross-sectional scanning electron microscope (SEM) micrograph of the cell is shown in Figure 1, together with an exemplary overlay of the oxygen partial pressure distribution during SOEC operation and the corresponding chemical expansion of the GDC. Using an adapted model to

calculate the chemically-induced elastic stresses in the multilayer system, we find that fuel cell operation induces sub-critical stresses in the electrolyte layer, which are further reduced with decreasing cell voltage, while electrolysis operation can induce high tensile stresses in the electrolyte that exceed the materials tensile strength. Interestingly, the calculated stresses for the investigated show a maximum at 750 °C, which is verified experimentally. The explanation can be found in the competing effect of the respective temperature dependence of the fuel electrode polarization and the reducibility of ceria. Overall, our work shows that thin, supported ceria electrolytes are much more tolerant toward electro-chemically induced stresses than has previously been suggested.

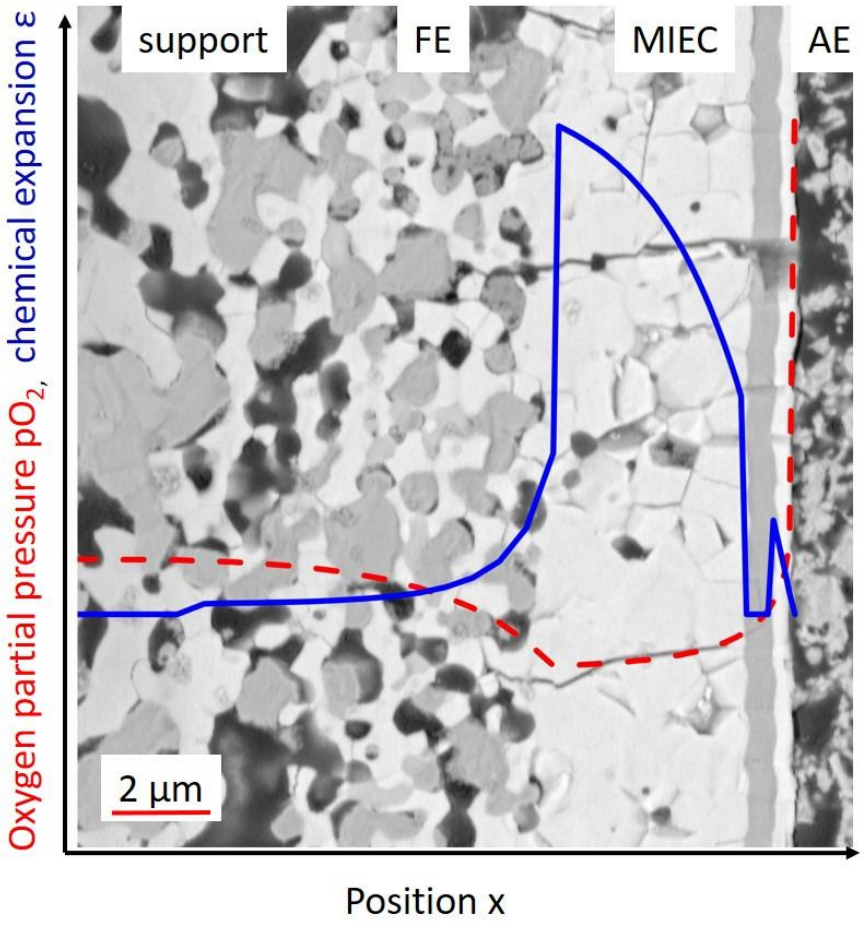

Figure 1: SEM micrograph of a cell cross-section, showing the Ni-YSZ support, the Ni-GDC fuel electrode (FE), the three-layer electrolyte (MIEC), and the air electrode (AE). The dashed, red line shows a the oxygen partial pressure distribution during SOEC operation (at 750 °C and at -2 Acm^{-2}), and the blue line the calculated chemical expansion of the ceria.

2. Materials & Methods

2.1. Chemical expansion in ceria

Concerning its use as an electrolyte material, an important aspect of doped ceria ($Ce_{1-x}M_xO_{2-(x/2)-\delta}$, where M is a trivalent dopant) is the dependence of the oxygen non-stoichiometry δ on the electrochemical potential of oxygen ions $\bar{\mu}_{O^{2-}}$.[10] Since ceria is readily reduced at elevated temperatures, the material properties of ceria depend on both temperature and oxygen partial pressure. A first approximation of the dependence of non-stoichiometry on oxygen partial pressure can be derived from the law of mass action as $\delta \sim {pO_2}^{-1/4}$. More detailed investigations show that this is only valid for isolated oxygen vacancies, and that oxygen vacancy complexes (where vacancies associate to dopant ions) show a somewhat different pO_2-dependence, in such a way that the true dependence of δ on pO_2 shows different slopes in different pO_2 regimes.[5]

The increasing oxygen non-stoichiometry leads to an increase in the electronic charge carrier density,[11] and to an expansion of the lattice parameter due to the larger ionic radius of the Ce^{3+} ions.[5, 12] In analogy to thermal expansion, this expansion can be described by a coefficient of chemical expansion (CCE)

Equation 1

$$\alpha_{chem} = \frac{1da}{ad\delta}$$

where *a* is the unit cell parameter and $\delta$the non-stoichiometry parameter in the formula of GDC. As shown by Bishop, the exact value of α_{chem} depends on the relative fractions of oxygen vacancies (isolated, dimers, trimers), and therefore is a function of temperature and oxygen partial pressure. However, typical values for GDC10 range between 0.08 and 0.14 for temperatures between 800 °C and 700 °C.[13] Atkinson used a value of $\alpha_{chem} = 0.119$ to calculate stresses in a GDC membrane.[6] For the purpose of this work, the chemical expansion as a function of log pO_2 is approximated by fits to literature data (graciously provided to the authors by Sean Bishop).[12] The fits are shown in Figure 2. As will be discussed later, the lack of

available data at the most reducing conditions (which can only be reached by electrochemical reduction) is a severe problem for the accuracy of the model.

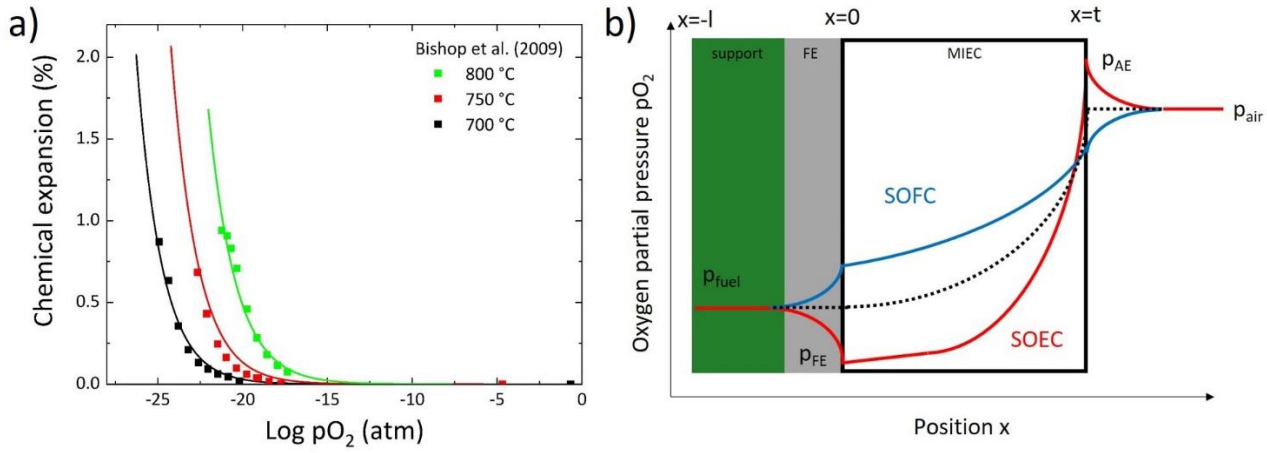

Figure 2: a) chemical expansion vs log pO2 for GDC10. Data from[12] with permission from the authors. b) Schematic representation of the oxygen partial pressure across an SOEC (red line) and an SOFC (blue line). The dashed, black line illustrates the hypothetical gradient across the electrolyte of a cell with reversible electrodes at OCV conditions.

2.2. Electrochemical potential

In an electrochemical cell, charged species are influenced by the electrical potential Φ, in such a way that the electrochemical potential of oxygen ions, $\bar{\mu}_{O^{2-}}$, is the sum of the chemical potential $\mu_{O^{2-}}$ and the electrical potential Φ:

Equation 2

$$\bar{\mu}_{O^{2-}} = \mu_{O^{2-}} - 2F\Phi$$

This is particularly relevant in solid oxide cells, since they have gradients in both the chemical and electrical potential of oxygen ions. The oxygen partial pressure and the electrical potential can be linked via an effective oxygen partial pressure, $pO_{2,eff}$, which can be calculated according to

Equation 3

$$\eta = -\frac{RT}{4F} ln \frac{pO_2}{pO_{2.eff}}$$

where η is the applied potential difference, R the ideal gas constant, T the absolute temperature, F is Faradays constant, and pO_2 is the reference pO_2 established by the gas atmosphere. Using Equation 3, the effect of applied overpotentials can be included in the pO_2 gradient across an electrochemical cell. This equates to a simplification that the electrode overpotentials are assumed to be ohmic.[6]

2.3. Spatial distribution of oxygen non-stoichiometry in a ceria electrolyte with non-reversible electrodes

Figure 2 b) shows a schematic representation of the oxygen partial pressure gradient in an SOC with an MIEC electrolyte for three different scenarios. The oxygen partial pressure in fuel and air are denoted as p_{fuel} and p_{air}, respectively, and determine the gradient across the electrolyte membrane. The dashed, black line shows the hypothetical case for an SOC under open circuit voltage (OCV) with reversible electrodes (no electrode overpotential). The solid blue line represents the case of fuel cell operation with electrode polarization, whereas the red line represents the case of electrolysis operation. It can be seen that the electrode polarization influences the oxygen partial pressure at the interfaces between the electrodes and the electrolyte. In SOFC mode, the electrode polarization will decrease the pO_2 gradient across the electrolyte, while it will be amplified in SOEC mode.[14] The gradient of the oxygen chemical potential inside the mixed ionic and electronic conducting electrolyte was calculated by Riess *et* al.. [15] Gödickemeier *et* al. later derived an expression for the chemical potential of oxygen across an MIEC membrane of thickness *t* as:[16]

Equation 4

$$\frac{\mu_{O_2}(x)}{\mu_{O_2}(0)} = -4\mathrm{kT}\ln\left\{\left(1 - exp\left(-\frac{eV_{th,MC}}{kT}\right)\frac{1-exp\left(-\frac{e(V_{th,MC}-V_{MC})\frac{x}{t}}{kT}\right)}{1-exp\left(-\frac{e(V_{th,MC}-V_{MC})}{kT}\right)}\right)\exp\left(-\frac{e}{kT}\eta_{FE}\right)\right\}$$

where μ_{O_2}*(0)* is the chemical potential of oxygen in the fuel atmosphere, $V_{th,MC}$ is the Nernst voltage across the mixed conductor, V_{MC} is the voltage drop across the mixed conductor, t is the electrolyte thickness, and e is the elementary charge, and η_{FE} is the fuel electrode overpotential. $V_{th,MC}$ deviates from the Nernst voltage V_{Nernst} by the electrode overvoltage as $V_{th,MC} = V_{Nernst} - \eta_{trode}$. V_{MC} is the difference between the cell voltage and the electrode overpotential: $V_{MC} = V_{Cell} - \eta_{trode}$.

With $\mu_{O_2} = kTln(p_{O_2})$, the oxygen activity can be converted into an equivalent partial pressure. The value of μ_{O_2}*(0)* is calculated from the pO_2 of the fuel gas, which in turn is calculated via the Nernst equation at OCV:

Equation 5

$$V = OCV = -\frac{RT}{4F}ln\left(\frac{pO_{2,fuel}}{pO_{2,air}}\right)$$

The total electrode overpotential at the electrode/electrolyte interfaces, η_{trode}, at every working point is calculated via

Equation 6

$$\eta_{trode} = OCV - V_{cell} - R_{lyte}I_{cell}$$

Where V_{cell} denotes the (external) cell voltage, OCV the open circuit voltage, R_{lyte} the ohmic resistance of the electrolyte (determined from the impedance spectra at OCV), and I_{cell} the total current through the cell. The sum of the overpotentials at the fuel electrode (FE) and air electrode (AE) equate to the total electrode overpotential:

Equation 7

$$\eta_{trode} = \eta_{FE} + \eta_{AE}$$

Since the individual values of the electrode overpotentials are unknown during cell operation at this point, a simple relation is used to connect the unknown overpotential at the fuel electrode (η_{FE}) to the known electrode overpotential (η_{trode}):

Equation 8

$$\eta_{trode} = \beta \cdot \eta_{FE} + (1 - \beta) \cdot \eta_{AE}$$

By varying β, the model can capture the influence of the respective overpotentials on the oxygen chemical potential profile in the MIEC at a given operation point.

While Equation 4 can be used to determine the chemical potential of oxygen (and therefore the amount of chemical expansion) in the electrolyte, the doped ceria contained in the fuel electrode also undergoes chemical expansion. The chemical potential of oxygen on either side of the fuel electrode is determined by the fuel gas on the one side, and the value of μ_{O_2} at the fuel electrode / electrolyte interface on the other side. The gradient of η_{FE} is modelled under the assumption of an exponential decay of the ionic current in the electrode as a function of distance from the electrolyte:[17]

Equation 9

$$\eta_{FE}(x) = \eta_{FE,0} * exp\left(-\frac{x}{\lambda}\right)$$

where λ is the penetration depth. Note that λ is a specific quantity for a given electrode, as it reflects the square root of the ratio of the charge-transfer resistance and the ionic resistance in the electrode. For the sake of simplicity, a value of λ = 2 µm was arbitrarily chosen for this study, which means that (almost) all electrochemical activity will take place in the electrode of an assumed 7 µm thickness. Equation 9 also assumes ohmic behavior of the electrode, i.e. that the current and overpotential are linearly connected.

For GDC, this not quite accurate since the conductivity and electrochemical activity are a function of the pO_2, but this is neglected in the current model and is expected to lead only to minor changes in the overall results.

For part of this analysis, the air electrode is treated as reversible (pO_2,air = pO_2,AE; $\beta = 1$). In practice, $pO_{2,AE} > pO_2$,air due to the cathode polarization in SOEC mode. It is important to point out that the $pO_{2,AE}$ does not contribute significantly to the chemical expansion of the ceria electrolyte, therefore it is an acceptable simplification to set pO_2,air = $pO_{2,AE}$.

2.4. Chemical stresses in an elastic multilayer system

The analysis of thermal stresses in elastic multilayer systems by Hsueh treats the thermal stresses - occurring due to mismatches in coefficients of thermal expansion in a supported multilayer system - as a linear superposition of the individual layers.[18] Here, this approach is adjusted to include the chemical strain in the system:

Equation 10

$$\varepsilon = \varepsilon_{therm} + \varepsilon_{chem}$$

In the present case, we consider an isothermal situation ($\varepsilon_{therm} = 0$). Therefore, all terms relating to thermal expansion can be eliminated from the equations, and ε_{chem} will be written as ε for simplicity.

To model electro-chemo-mechanical stresses in a fuel electrode-supported SOEC, we consider a model that consists of a support with thickness t_s and a number i of layers with thickness t_i, with a total layer thickness t as sketched in Figure 3. The support extends from the ordinate $-t_s$ to 0, and therefore $t = \sum_{i=1}^{n} t_i$. The total height on top of each layer h_i is the sum of the thickness of each layer t_i: $h_i = \sum_{j=1}^{i} t_i \quad (i = 1\ to\ n)$. The unconstrained strains in each layer ε_i and the substrate ε_s are calculated individually, and subsequently uniform stress is applied to each layer in order to attain displacement

compatibility and the strain is uniform throughout the system. Finally, the system is permitted to bend due to any asymmetric stress distribution.

In this way, the strain in each layer is a combination of the uniform strain *c* and the strain induced by bending:

Equation 11

$$\varepsilon = c + \frac{x - t_b}{r}$$

where x is the spatial coordinate, $x = t_b$ marks the location of the bending axis and r is the radius of curvature of the system. The extension of the support is from x = -l to x = 0, as shown in Figure 2 b)**Fehler! Verweisquelle konnte nicht gefunden werden.**.

The stress at each coordinate can then be calculated through Hooke's law

Equation 12

$$\sigma_s = E_s(\varepsilon - \varepsilon_s) \qquad \text{(for } -l \leq x \leq 0\text{)}$$

$$\sigma_i = E_i(\varepsilon - \varepsilon_i) \qquad \text{(for } 0 \leq x \leq t\text{)}$$

for the support *s* and each layer *i*, using the corresponding values for the biaxial Young's modulus E_i and the strain ε_i at position *x*. The corresponding equations for a system of *n* layers with thickness t_i are:

Equation 13

$$c = \frac{E_s t_s \varepsilon_s + \sum_{i=1}^{n} E_i t_i \varepsilon_i}{\sum_{i=1}^{n} E_i t_i}$$

Equation 14

$$t_b = \frac{-E_s t_s^2 + \sum_{i=1}^{n} E_i t_i (2h_{i-1} + t_i)}{2\left(E_s t_s + \sum_{i=1}^{n} E_i t_i\right)}$$

Equation 15

$$\frac{1}{r} = \frac{3\left[E_s(c-\varepsilon_s)t_s^2 - \sum_{i=1}^{n} E_i t_i (c-\varepsilon_i)(2h_{i-1}+t_i)\right]}{E_s t_s^2 (2t_s+3t_b) + \sum_{i=1}^{n} E_i t_i [6h_{i-1}^2 + 6h_{i-1}t_i + 2t_i^2 - 3t_b(2h_{i-1}+t_i)]}$$

Since this formulation is valid for uniform values of ε, it is necessary to introduce a formalism to include gradients of ε as ε(x). Since the formalism relies on a summation of each individual layer, the correct approach would be to include gradients in ε(x) by integrating the value of ε across each layer as $\varepsilon_i = \int_{x=h_{i-1}}^{h_{i-1}+t_i} \varepsilon(x)$. As an alternative, one can determine the distribution of the chemical potential of oxygen $\mu_{O_2}(x)$ according to Equation 4, then divide the electrolyte into a number of discrete layers and assign each layer the value of $\varepsilon_i = \varepsilon(h_i)$. We use the latter method and divide the electrolyte to consist of 45 layers, each 0.1 µm thick as shown in Figure 3. This amounts to a numerical integration and yields accurate results if the chosen number of layers is sufficiently high. In the present study, doubling the amount of layers in the electrolyte changed the value of maximum tensile stress by 0.1%, demonstrating the robustness of the chosen parameters.

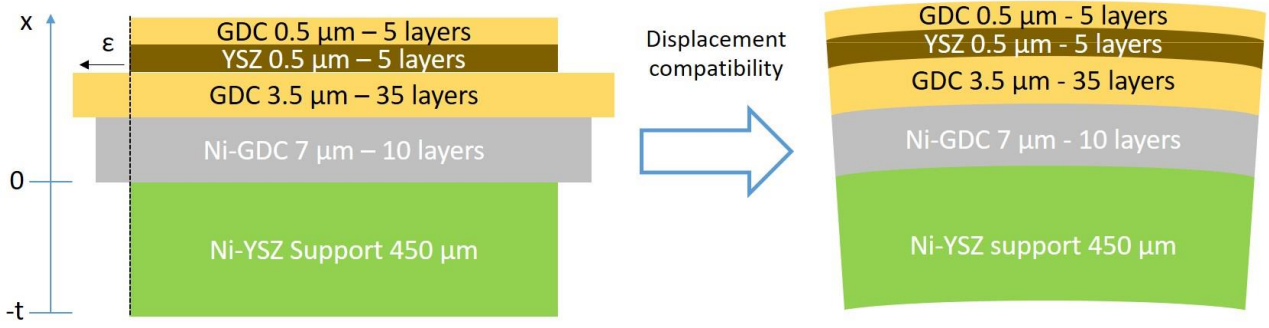

Figure 3: sketch of the model used for the calculation for the chemical stresses in the multilayer system

Table 1 shows a survey of material properties from various sources in the literature. The processing method of the ceramic, the purity of the powder, the grain size distribution, pore fraction and various other factors influence the mechanical properties of ceramics, therefore there are discrepancies between individual investigations. The values chosen for these calculations are printed in bold. These values were

chosen since they were judged to most accurately reflect the investigated system in this work. The sensitivity of the results to the chosen values will be briefly discussed at the end of this work. For reasons of simplicity, the air electrode was omitted from the calculations of elastic stresses. It is expected that the air electrodes do not stabilize the cell in a significant manner due to its high porosity and low mechanical strength.

The expansion of the GDC electrolyte layers is calculated via $\mu_{O_2}(x)$ and the fits to the experimental data shown in Figure 2 a). For the Ni-GDC anode, a factor of 0.33 was introduced for the expansion under the assumption that the volume of the fuel electrode consists of roughly 1/3 GDC, 1/3 Ni and 1/3 porosity. Changing this factor to 0.5 increases the maximum tensile stress in the electrolyte by about 5%, showing that the analysis is relatively insensitive to this factor.

All stresses are calculated relative to a stress-free state of the cell at pO_2 = 0.21 atm. This means that stresses induced by the reduction of the substrate, as well as residual stresses after fabrication, are neglected in the present analysis.

Table 1: A survey of material properties from the literature

Material	Young's modulus (GPa)	Poisson's ratio	Atmosphere	Temperature (°C)	Flexural strength (MPa)	Ref.
8YSZ			Air	950	256	[19]
	200		Air	RT	200	[20]
	140		Air	800		[21]
			Air	800	237 $\pm$ 30	[22]
			Air	RT	278 $\pm$ 59	[23]
	150		Air / 99% H_2	800		[24]

	157	**0.313**	Air	800	146	[13]
10GDC	260		Air	RT		[25]
	190		$pO_2 = 10^{-24}$ atm	RT		[25]
	170		0.01% O2	800		[24]
	140	**0.31**	99.15 % H_2/H_2O	800		[24]
Ni-3YSZ	30.7 $\pm$ 1.4	0.28	9% H_2 in N_2	800		[26]
	40.9 $\pm$ 2.8		9% H_2 in N_2	600		[26]
Ni-8YSZ	57	**0.28**	Not specified			[27]
	23.8		H_2	800		[28]

2.5. Constraint conditions

Equation 13 - Equation 15 are derived through a balance of forces in the system, such that the sum of the forces induced by the uniform strain and the bending are equal to zero, and that the sum of the bending moment is equal to zero with regard to the bending axis.[18] This amounts to a system that is free to bend and deform. In practice, however, the multilayer system (here an SOC) is constrained in some form. The conceivable cases are

i) Constrained flat: the cell can expand in a lateral direction, but cannot bend due to stiff current collectors. This condition is trivially satisfied by demanding that $1/r = 0$.

ii) Rigid seal: the cell cannot move laterally due to a rigid, hard seal around the cell, but it can bend. This is trivially satisfied by $c = 0$.

iii) Totally constrained: the cell can neither expand nor bend. This can be trivially achieved by setting $c = 0$ and $1/r = 0$. It should be noted that in this case, all stresses are compressive since no expansion can take place. This is sometimes assumed to be the case when considering a thin membrane supported by a porous substrate.[13]

In practice, which condition is the most realistic is not a simple question. Case iii) may be most appropriate for a Jülich F10 stack with crystallized glass-ceramic sealant around the cell and thick, stainless steel current collectors with a strong mechanical loading on the stack. However, it is worth noting that the stresses induced into the electrolyte by anode re-oxidation (which is mechanistically similar to the case discussed here) are able to induce cracking in the electrolyte even in an F10 stack, where a totally constrained cell would only experience compressive stresses in that situation. Logically, some deformation must be possible even with a glass ceramic sealant and thick Crofer interconnects (although the larger cell plays a role as well).

The experimental results shown in this work were obtained on a cell mounted in a test rig inside an alumina housing and sealed with a Au ring.[29] Since the Au ring is rather ductile at 800 °C and the cell is not specifically weighed down in order to keep it flat, the cell will be treated as free to deform in this work and the majority of the results will be shown for the unconstrained case. The effect of the three constraint conditions will be discussed as well.

3. Experimental

3.1. Cell manufacturing

The NiO-GDC fuel electrode was screen printed on a 450 µm thick NiO-8YSZ support [30] and pre-sintered. A GDC electrolyte layer was deposited via screen printing, the half-cell was sintered to final density at 1400 °C for 5 hours. First a 0.5 µm thin 8YSZ layer was deposited by electron-beam evaporation of 8YSZ targets, and subsequently a 0.5 µm GDC layer was deposited via magnetron sputtering. Finally, the $La_{0.58}Sr_{0.4}CoO_{3-\delta}$ air electrode was screen-printed and sintered at 850 °C for 3 hours in air. Details on the manufacturing route of the tested cells will be published elsewhere.

3.2. Cell testing

The cell testing was performed in single test benches at KIT. Details on the test benches, contacting and sealing concepts, cell layout and testing procedures can be found in [29, 31]. The cell was contacted by an Au mesh on air side and by a Ni mesh on fuel side. Resulting contact resistances were found to be negligible [32]. After sealing the cell with Au-frames at 900°C, the reduction of the fuel electrode was performed according to a defined procedure. After a run in procedure (1 A/cm², SOFC-mode, 24h) CV-characteristics and impedance spectra were measured at varied operating conditions in SOFC and SOEC mode. A detailed impedance and DRT analysis [33] required for the parameterization of advanced electrochemical models [34, 35] was not performed for this cell so far.

3.3. Post-test analysis

After cell testing, the microstructure of the cells was analyzed using scanning electron microscopy (SEM, Zeiss ULTRA 55, Oberkochen, Germany) on fractured or polished cross-sections. To prepare polished cross-sections, the cells were embedded in resin, ground using SiC sandpaper and polished with diamond paste.

4. Results

4.1. Cell test

The current-voltage characteristics of the cell are shown in Figure 4 in SOEC and SOFC mode using air as oxidant and 56% H_2O / 44% H_2 as fuel. The measurements were performed in SOFC mode first, then in SOEC mode. The cell shows an excellent performance and delivers a current density of 1.96 A·cm^{-2} at a cell voltage 800 mV (corresponding to a voltage efficiency of $\eta_{Cell} = \frac{V_{cell}}{EMF}$ = 86.3 %), and an electrolysis current

density of -1.94 A·cm^{-2} at a voltage of 1100 mV at 800 °C (both with a relative humidity of 56% in the fuel gas). With 12% relative humidity in the fuel gas, the cell delivers 1.9 A·cm^{-2} at a cell voltage of 800 mV at 700 °C. These values compare very favorably to the best results reported in literature, especially considering that testing conditions are rarely identical.[36]

The I-V curves at 800 °C and 750 °C show no obvious signs of degradation. However, after SOEC operation at 750 °C, the OCV at 700 °C is decreased significantly compared to the value at 750 °C, indicating an increased leakage in the electrolyte. Since the humidity is already very high, this leakage must be substantial. While SOFC operation at 700 °C shows no irregularities, the SOEC voltage shows an abrupt jump at a current density -1.68 A cm^{-2}. Measurements at 650 °C showed a further decrease of OCV. Further characterization down to a temperature of 450 °C (not shown) showed no signs of additional degradation. However, a decrease of OCV with decreasing temperature was noticeable, contrary to thermodynamic predictions for the electromotoric force and a clear indicator for a damaged cell.

A second cell tested under comparable conditions showed the same behavior of decreased OCV after SOEC operation at 750°C, and an abrupt voltage increase at 700 °C at a current density of -1.25 A cm^{-2}. A third cell was tested under SOFC conditions only, and showed no signs of damage.

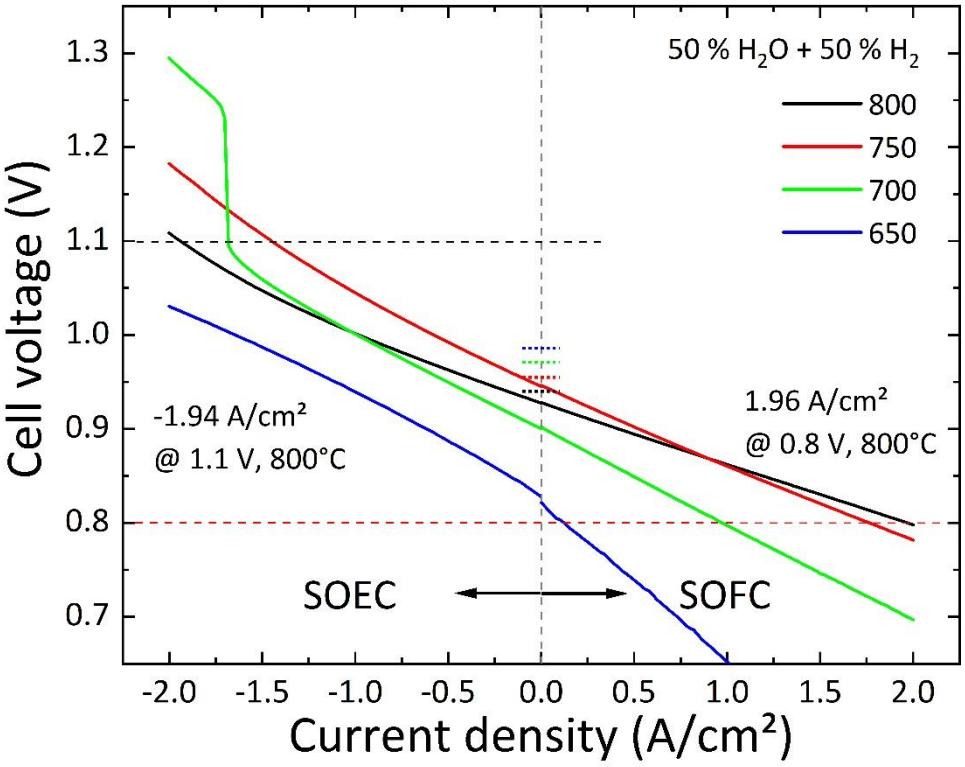

Figure 4: Current-voltage curves as a function of temperature at a fuel composition of 50% H_2O and 50% H_2. The theoretical OCV values are shown as dashed lines for each temperature.

Table 2 summarizes the parameters used for the calculations of the mechanical stresses. These parameters where extracted from impedance characterization at OCV (ASR_{ohm}) and the cell tests (OCV, ASR), or calculated from these values. Note that the OCV value at 700 °C for SOEC mode is 0.9 V, representing the damaged cell, whereas for SOFC calculations, the OCV value of 0.957 V of the intact cell was used. The theoretical OCV calculated from the nominal gas composition of the fuel is given as OCV_{theo}.

Table 2: Electrical parameters used for the simulations.

Temperature (°C)	Current (A cm^{-2})	η (V)	R_{pol} (mΩ cm^2)	pO_2_fuel (bar)	pO_2_FE (bar)	OCV / OCV_{theo} (V)	ASR_{ohm} (mΩ $cm^{2)}$
800	0	0	--	7,98 E-19	7,95 E-19		5

	-0,5	-0,0335	67		1,87 E-19	0.927 / 0.94	
	-1	-0,068	68		4,21 E-20		
	-1,5	-0,1125	75		6,15 E-21		
	-2	-0,173	86,5		4,49 E-22		
750	0	0	--	4,97 E-20	4,95 E-20	0.945 / 0.955	7
	-0,5	-0,0435	87		6,9 E-21		
	-1	-0,093	93		7,3 E-22		
	-1,5	-0,1515	101		5,14 E-23		
	-2	-0,221	110,5		2,19 E-24		
700	-0,5	-0,0435	87	4,7 E-20	5,9 E-21	0.9* (0.957) / 0.971	11
	-1	-0,089	89		6,73 E-22		
	-1,5	-0,1435	95,7		5 E-23		
	-1,68	-0,17552	104,5		1,08 E-23		

4.2. Post-test analysis

After testing, cross-sectional imaging of the cells was performed on both fractured and embedded specimens. Figure 5 a) shows a fractured cross-section of the electrolyte and the two electrode / electrolyte interfaces. Two large cracks in the electrolyte are clearly visible (indicated by the red arrows), running parallel to the direction of the oxygen chemical potential gradient in the cell during operation. The interface of the Ni-GDC fuel electrode to the support shows an increase in porosity, which is probably a result of interdiffusion during cell manufacturing.[4] Figure 5 b) shows the electrolyte and both electrode

/ electrolyte interfaces at a higher magnification, highlighting that both electrodes appear to be well-connected to the electrolyte.

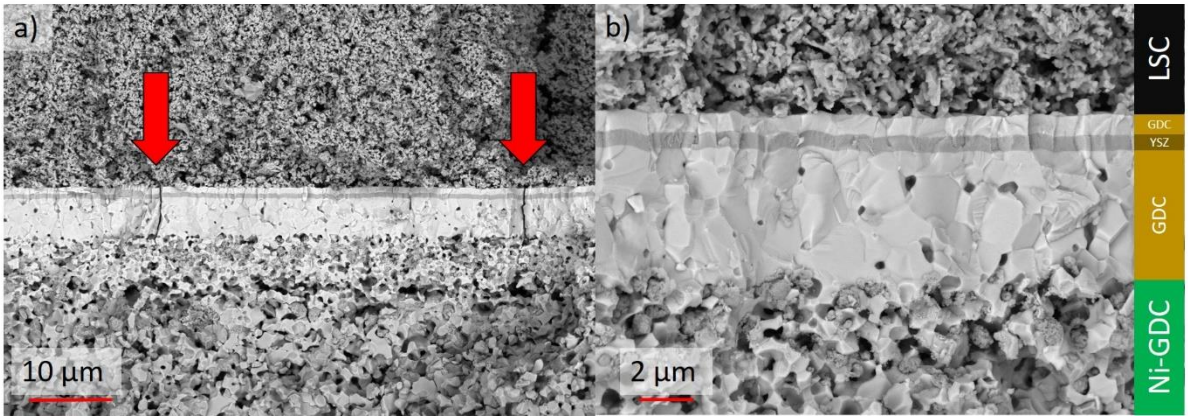

Figure 5: SEM micrograph of a fracture cross-section of the tested cell at a) low and b) high magnification. The detected signal are backscattered electrons (BSE).

However, the fuel electrode shows signs of re-oxidation, since the Ni grains appear sponge-like and with rough surfaces. This is likely a result of oxidation during cooldown, since the cell voltage was kept above 600 mV at all times during the cell test to avoid electro-chemical re-oxidation of the Ni. Figure SI 1 emphasizes that damage to the electrolyte is confined to the active cell area during cell testing, and that the cell area without any air electrode does not show signs of cracking.

The large cracks in the electrolyte are the most likely explanation for the decreasing cell voltage during cell testing, since they can be expected to lead to a dramatic increase in fuel humidity. For instance, the OCV at 500 °C was 800 mV, corresponding to a relative humidity of 99.9% in the fuel gas, while the relative humidity at 800 °C and 750 °C was 56% (OCV = 927 mV and 945 mV, respectively).

An important observation is that cracking only occurs in the active cell area. This suggests that the stresses resulting in crack formation are induced during electrolysis operation and are a result of electro-chemo-mechanical coupling. This hypothesis is supported by the fact that fuel cell operation did not lead to cell failure, and that cell damage is confined to the active cell area.

4.3. Electro-chemo-mechanical modelling

In order to test the hypothesis that electrolysis operation leads to cracking in the electrolyte, the elastic stresses were calculated for three temperatures (700 °C, 750 °C, 800 °C) and four current densities for each operation mode (±0.5 $A \cdot cm^{-2}$, ±1 $A \cdot cm^{-2}$, ±1.5 $A \cdot cm^{-2}$ and ±2 $A \cdot cm^{-2}$) as well as under open circuit voltage. All current-voltage values used for the calculations are from the same cell, although it bears pointing out that these values have been reproduced with two further cells. For the stress calculation at OCV and in SOFC mode at 700 °C, the used values were measured before the cell was damaged. The values in SOEC mode at 700 °C are taken from the damaged cell.

4.3.1. Ni-YSZ support

Figure SI 2 shows the calculated oxygen partial pressure profiles (dashed lines) and the corresponding unconstrained, elastic stress (solid lines) for all three temperatures under OCV in the entire cell. The pO_2 is constant in the support (which extends from x = - 450 µm to x = 0 µm), and there is a transition from tensile stress at the gas-phase interface to compressive stress at the interface to fuel electrode. The stress is small (< 5 MPa) as a result of the cell curvature. Since these results are fairly consistent for all conditions, the support will mostly be left out of the discussion.

4.3.2. Fuel cell operation

For the calculations in this section, the entire electrode polarization has been attributed to the fuel electrode (β = 1 in Equation 8). The influence of β will be evaluated in section 4.3.4.

Figure 6 shows the pO_2 gradients and elastic stresses in the active layers of the cell (note the different scale of the stress in SOFC and SOEC mode). The interface between fuel electrode and support is located

at x = 0 µm, and the interface between fuel electrode and electrolyte at x = 7 µm. The first electrolyte layer is 3.5 µm thick, so that the bottom and top interface of the YSZ layer is located at x = 10.5 µm and x = 11 µm. The final GDC layer is also 0.5 µm thick, so that the interface to the air electrode is located at x = 11.5 µm.

Under OCV, the pO_2 is constant in the fuel electrode. This is a simplification since the electrodes in the real cell show some overvoltage even under OCV, but this is negligible compared to the overvoltage during operation and is therefore neglected. Nevertheless, the low pO_2 causes some expansion in the fuel electrode, resulting in a small compressive stress that increases with increasing temperature.

The pO_2-gradient in the electrolyte shows the typical shape for mixed-conductors, increasing very sharply towards the air electrode interface. The positive gradient means that the expansion of the GDC electrolyte layer is largest at the interface to the fuel electrode, and decreases with increasing pO_2. Correspondingly, the compressive stress in the GDC layer is largest at the fuel electrode interface, and increases with increasing temperature due to the temperature dependence of the equilibrium non-stoichiometry (higher reducibility) of GDC.

The stress changes sign at the interface to the YSZ layer. Since the YSZ layer shows no chemical expansion, it is under tensile stress due to the expansion of the underlying GDC layer. This stress is somewhat higher at the top interface due to the curvature of the cell. The magnitude of tensile stress in the YSZ layer is directly proportional to the expansion of the GDC layer underneath (and to a lesser extend of the Ni-GDC electrode). At 800 °C, the tensile stress under OCV reaches 37 MPa. The magnitude of stress is reduced in the top GDC layer, but the sign does not change and the stress remains tensile. Compared to the YSZ, the tensile increases much more over the layer thickness due to the changing pO_2. At the interface to the air electrode, the tensile stress in the top GDC layer reaches 32 MPa under OCV at 800 °C.

Figure 6 a), c) and e) show the pO_2-gradient and the stress in the active layers of the cell in fuel cell mode for 800 °C, 750 °C and 700 °C, respectively, for current densities between 0 and 2 A·cm^{-2} each. The effect of the fuel electrode overvoltage η_{FE} is clearly discernible, resulting in an exponential increase of the pO_2 values in the Ni-GDC electrode between x = 0 and x = 7 µm. Since the pO_2 increase is proportional to η_{FE} as formulated in Equation 3, the effect of overpotential on pO_2 is largest at 700 °C and smallest at 800 °C. Accordingly, the small compressive stress that is observed in the fuel electrode at each operation condition increases with temperature due to the temperature dependence of the equilibrium non-stoichiometry and decreases with the local value of η_{FE}, and peaks at 14 MPa at 800 °C under OCV.

The pO_2 gradient across the electrolyte layer is significantly reduced by η_{FE} in SOFC mode, by as much as 4 orders of magnitude at 700 °C and 2 A·cm^{-2} (compared to OCV). As a consequence, the compressive stress in the bottom GDC layer and the tensile stress in the YSZ / top GDC layer decrease with increasing η_{FE} (and increased current density). At the same time, the chemical expansion of GDC at a given pO_2 decreases with decreasing temperature, and both effects (decreasing chemical expansion and increasing electrode overvoltage) work together to reduce the magnitude of stress in the cell at lower temperatures.

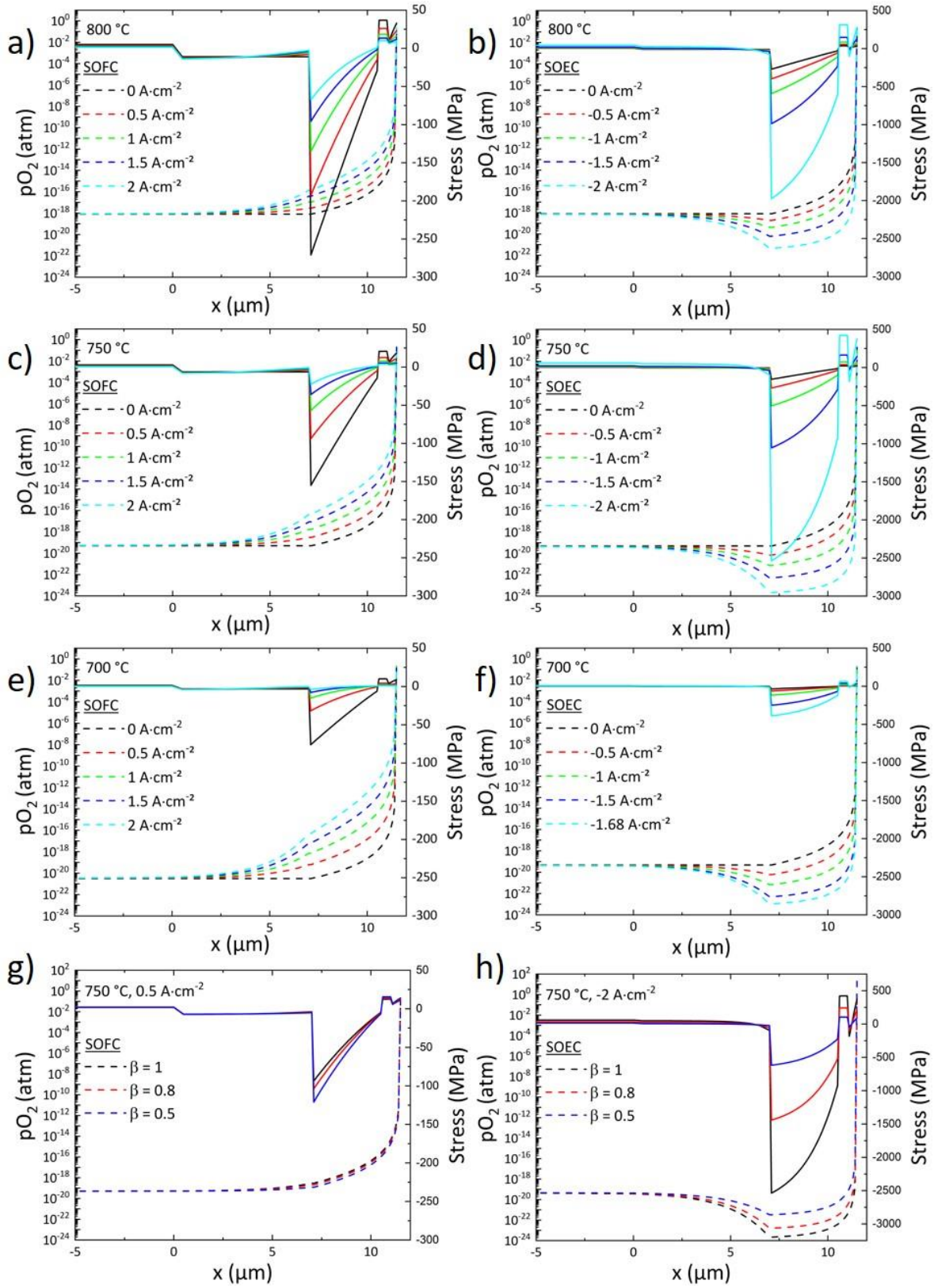

Figure 6: pO_2 (dashed lines) and stress (solid lines) plotted vs position x at 800 °C, 750 °C and 700 °C for SOFC operation (a), c) and e), respectively) and for SOEC operation (b), d) ,f) respectively). Note that the stress-scale is different by a factor of 10 between fuel

cell and electrolysis operation. Figure 6 g) and h) show the effect of the fuel electrode polarization for SOFC and SOEC operation, respectively, at 750 °C.

4.3.3. Electrolysis operation

Figure 6 b), d) and f) show the pO_2-gradient and the stress in the active layers of the cell in electrolysis mode for 800 °C, 750 °C and 700 °C, respectively, for current densities between 0 and -2 A·cm^{-2}. Note the different scale compared to fuel cell mode. Also in electrolysis mode, the effect of the fuel electrode overvoltage is pronounced, but the sign of the overvoltage is reversed with respect to fuel cell mode and accordingly, the pO_2 decreases through the thickness of the fuel electrode and reaches a minimum at the fuel electrode / electrolyte interface. In other words, the most reducing conditions (and hence, the highest expansion of GDC) are located right at the of fuel electrode / electrolyte interface. As a consequence, the compressive stress in the bottom GDC layer and the tensile stress in the YSZ / top GDC layer increases with increasing η_{FE}.

In contrast to fuel cell mode, the increasing η_{FE} works against the decreasing chemical expansion ε_{chem} (at a given pO_2) with decreasing temperature. ε_{chem} and η_{FE} are not trivially connected, since the former is determined by the reduction enthalpy of the ceria electrolyte, whereas the latter can be determined by a variety of factors (e.g. the surface exchange coefficient and oxygen diffusion coefficient in the Ni-GDC electrode, and the microstructural properties of the electrode). As a consequence of this competing influence, it is conceivable that the tensile stress may show a maximum at a certain temperature (for a given current density).

In the present case, the tensile stress in the YSZ layer is higher at 750 °C than at 800 °C for electrolysis current densities below –1 A·cm², which means that the electrode overvoltage dominates the temperature dependence of the tensile stress. The increase of η_{FE} exponentially increases the stress in the electrolyte layer, such that the maximum tensile stress at 750 °C and -2 A·cm^{-2} is more than twice as high as for -1.5

A·cm^{-2} (422 MPa and 163 MPa, respectively) although the cathode overvoltage is only about 31% higher (221 mV and 152 mV, respectively).

The values shown for 700 °C in Figure 6 f) are calculated from the I-V data of the damaged cell before the abrupt voltage increase seen in Figure 4. The resulting stress therefore represents the damaged cell with OCV = 0.9 V, and not the stress that would be present in the undamaged cell at 700 °C. (While such data was used for the fuel cell mode calculations in Figure 6 e), no such data exists for electrolysis mode).

4.3.4. Influence of fuel electrode overpotential (β < 1)

The individual overvoltages of fuel and air electrode are not known at this point and only the total electrode overvoltage can be calculated from the I-V curve and the known ohmic resistance. Therefore, the influence of the ratio of the electrode overvoltages on the stress in the multilayer structure can be examined by variation of the parameter β in Equation 8. Essentially, this keeps the overall electrode overvoltage constant but divides it between the two electrodes. So far, the case of β = 1 was discussed (meaning that the complete electrode overvoltage drops at the fuel electrode), while setting β = 0.5 means that both electrodes have the same overvoltage. Figure 6 g) and h) show the results for β =1, 0.8 and 0.5 for two exemplary cases at 750 °C: SOFC operation at 0.5 A·cm^{-2} and SOEC operation at -2 A·cm^{-2}. In the case of fuel cell operation, decreasing β results in slightly higher stresses in the multilayer structure due to a slightly lower pO_2 in the MIEC. Note that this leads to a decreased pO_2 at the air electrode / electrolyte interface due to the air electrode overvoltage η_{AE}, which has been proposed as one explanation for the deposition of $SrCrO_4$ in this area of the electrode.[37] In contrast, decreasing β in electrolysis mode profoundly increases the pO_2 in the MIEC and correspondingly lowers the stress in the multilayer structure for decreasing β. At the same time, the pO_2 at the air electrode / electrolyte interface increases more than 2 orders of magnitude, up to pO_2 ~ 32 atm for β = 0.5. It has been hypothesized that the increased pO_2 at this interface can lead to air electrode delamination.[38] This degradation mechanism has not been

observed in the present study, most likely due to the fact that the air electrode overvoltage remains below a critical value that leads to delamination, which has typically been observed at lower temperatures or higher cell voltages than in the present study.[39, 40]

4.3.5. Maximum tensile stress

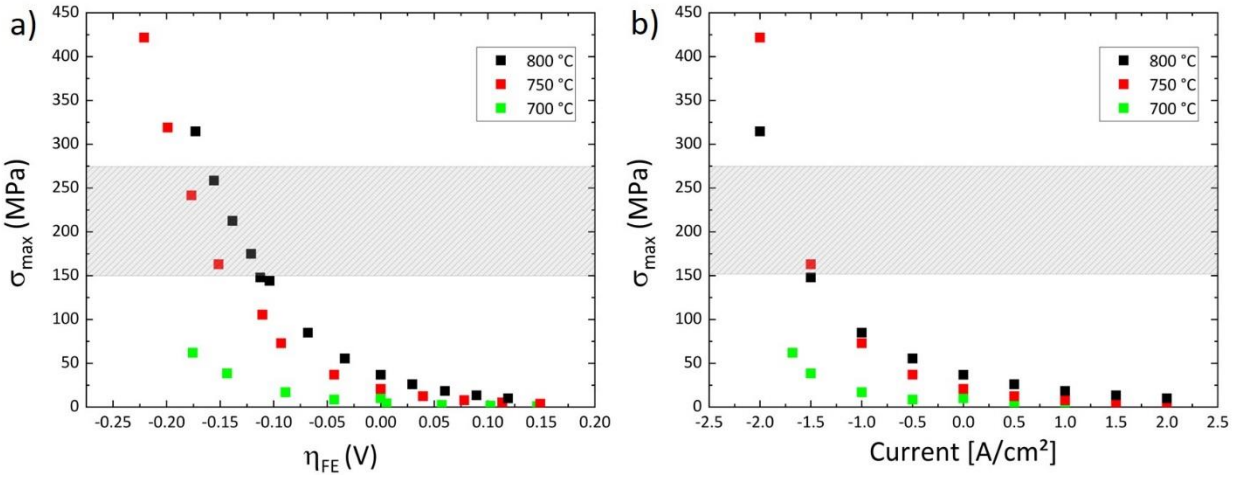

Figure 7: maximum tensile stress in the multilayer structure (always found in the YSZ layer) as a function of a) fuel electrode overpotential and b) current density. The shaded area indicates the range of plausible values for the tensile strength of YSZ based on literature values.

The highest values of tensile stress always occurs at the interface of the YSZ layer and the GDC layer on the air-side. The tensile stress is mainly caused by the curvature of the cell, and is almost constant across the YSZ layer due to its low thickness. The maximum values of tensile stress are shown in Figure 7 as a function of fuel electrode overvoltage (a)) and current density (b)). In a), η_{FE} = 0 is used to denote OCV. The shaded grey area indicates a plausible range of values for the tensile strength of 8YSZ, based on several studies in literature (see Table 1). We note that these values are recorded for bulk samples, and therefore may significantly underestimate the tensile strength of a very thin layer.

Figure 7 confirms the trends seen above: the maximum tensile stress increases with increasingly negative fuel electrode overvoltage in electrolysis mode, and decreases with increasingly positive fuel electrode

overvoltage in fuel cell mode. There is a clear temperature dependence, such that the stresses for a given electrode overvoltage are always highest for the highest temperature. This is a consequence of the increased equilibrium concentration of oxygen vacancies in the GDC. For a fuel electrode overvoltage of η_{FE} > -0.1 V at 800 °C and η_{FE} > -0.15 V at 750 °C, the tensile stress is well below the tensile strength of 8YSZ and damage to the cell is not expected. For increasingly negative η_{FE} at either temperature, the tensile stress in the YSZ layer approaches or surpasses the tensile strength of bulk 8YSZ.

The situation becomes clearer when considering Figure 7 b), which shows the tensile stress as a function of current density. Here, the tensile stress is lower at 750 °C then at 800 °C below a current density of -1 A·cm^{-2}, and for higher (more negative) current density the stress at 750 °C is higher than at 800 °C. This cross-over is the result of the competing influence of the reducibility of the ceria (which increases with temperature) and η_{FE}, which becomes larger with decreasing temperature at a given current density.

4.3.6. Effect of constraints

So far, all stresses have been calculated without any constraints on the cell deformation. As discussed in section 2.5, the cell is unlikely to be free of any such constraints in a cell test rig, or even a stack. Therefore, Figure 8 shows the effect of constraints imposed by external clamping for the four cases discussed in section 2.5, for the case of electrolysis operation at 750 °C and a current density of -2 A·cm^{-2}. The tensile stress in the YSZ layer is highest in the absence of any constraints (black line, σ_{max} = 422 MPa), and second highest for a cell that is allowed to bend (but not to expand laterally, green line, σ_{max} = 300 MPa). A cell that is constrained flat and cannot bend (blue line, σ_{max} = 122 MPa) shows some tensile stress in the YSZ, while the fully constrained cell does not show any tensile stress in the YSZ layer (red line, σ_{max} = 0 MPa).

Conversely, the maximum compressive stress in the cell (located at the fuel electrode / electrolyte interface) increases in the same order as the maximum tensile stress decreases. While it is possible that compressive stresses in the structure lead to delamination of the electrolyte from the fuel electrode, no

such behavior was observed in this study. However, this aspect should not be neglected and will be investigated further.

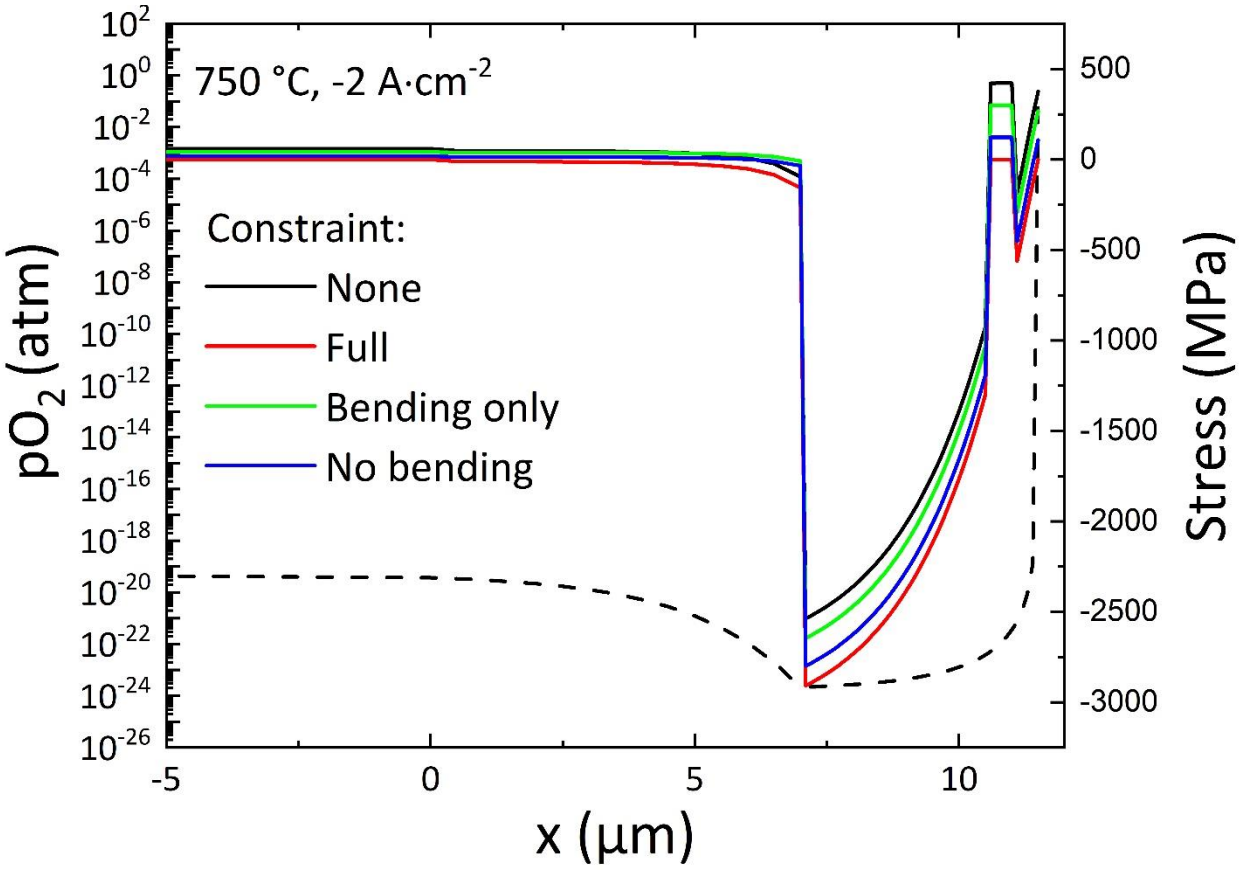

Figure 8: Effect of the 4 cases of constraints on the stress in the cell for electrolysis operation at 750 °C and -2 A·cm^{-2}.

5. Discussion

The calculation of elastic electro-chemo-mechanical stresses in the multilayer system of the cell showcases the influence of each layer on the resulting stress. The support acts as a clamp, and reduces the induced stresses in the active layers of the cell. The chemical expansion of the electrolyte is the main reason for induced stresses, since it is dense, purely made from doped ceria and exposed to the most reducing conditions in the cell in SOEC mode. The fuel electrode, despite containing ceria as well, shows much less expansion due to the presence of Ni and pores, which reduce the effective expansion coefficient.

The induced stresses are mostly compressive on the fuel side, since the chemical expansion of the electrolyte is prevented by the clamping effect of the support. Nevertheless, the cell bends without any external constraints, which induces tensile stresses in the air side of the electrolyte. In particular, the YSZ layer sandwiched between the two GDC layers does not show any chemical expansion despite the reduced local pO_2, and is therefore subjected to tensile stresses from the expansion of the underlying GDC layer. For the investigated system in electrolysis operation, these elastic tensile stresses can exceed the tensile strength of bulk YSZ, in good agreement with the experimental observation of cracks forming in the electrolyte.

An important finding is that the maximum tensile stress is positively correlated with two factors: the reducibility of GDC (more precisely, the equilibrium constant K^{red} for the reduction reaction) and the fuel electrode polarization η_{FE}. An increase in either of these two quantities increases the tensile stress. However, the temperature dependence of these two quantities is opposite, with the reducibility increasing and η_{FE} decreasing with increasing temperature. The result is that the maximum tensile stress in the multilayer system shows a maximum at a certain temperature, which is 750 °C in this study. This finding may serve as an explanation for why SOEC operation at 800 °C did not lead to cell failure, but operation at 750 °C did, which was observed in two separate cell tests.

Concerning fuel cell operation, the decreasing tensile stress with decreasing temperature on the air side is in line with the conclusions of other researchers who recommend to operate GDC electrolytes below a certain temperature. However, these studies predict stability criteria for electrolyte-supported cells,[6, 7] or do not quantify stress.[9] While our results confirm decreasing tensile stress with decreasing temperature in fuel cell mode, the highest, chemically-induced tensile stress (at 800 °C) occur under OCV and amounts to 37 MPa and is therefore likely sustainable for long operation times. Furthermore, fuel cell operation reduces the pO_2 gradient across the electrolyte, and therefore also the magnitude of the stress in the multilayer structure, which is beneficial for the cell lifetime in fuel cell mode. The difference of our

study to the aforementioned works is the quantitative integration of the stabilizing role of the support, which is very beneficial for cell stability compared to a free-standing electrolyte membrane.

Finally, it is necessary to discuss the shortcomings of the model used in this investigation. Like every model, it is dependent on some simplifications and assumptions. The most important ones are:

- The pO_2 dependence of Young's modulus of GDC has not been considered in this study. A lower Young's modulus would reduce the compressive stresses in the GDC layer. But since it would not reduce the strain, the tensile stresses in the YSZ layer would remain unchanged.
- The actual fuel electrode polarization is not known at each operation point. The values used as the basis for this study are reasonable deductions, but accurate calculations would require precise knowledge of η_{FE}.
- The mechanical constraints of the cell during testing are not known. While this study covers several exemplary cases, the actual constraint imposed by the setup may be a key to prevent cracking in the electrolyte. For instance, it is possible that rigid interconnects in an SOEC stack will help reduce the tensile stress during SOEC operation. Investigations in this direction are currently underway.
- The values for the chemical expansion of GDC at very low pO_2 are extrapolated values. This is due to the fact that such low values are inaccessible with chemical means (such as CO/CO_2 mixtures). Due to the fact that defect ordering can play an important role for high defect concentrations, these extrapolations should be treated with caution. Experimental efforts investigating the electro-chemical expansion of GDC under relevant conditions are needed to enable precise predictions of the stress.
- The residual stress in the multilayer system is not known. Residual compressive stresses in the electrolyte layer could have a beneficial impact for the stability, but more investigations are necessary to determine the residual stresses under operation conditions.

- In order to calculate the gradient of the chemical potential of oxygen through the electrolyte layer, the entire three-layer system has been treated as an MIEC. This is clearly not accurate in the case of YSZ. A more complex treatment would certainly complicate the model significantly, but it is unlikely that a segmented calculation of the μO_2 that treats the GDC and YSZ layers differently would yield drastically different results, since the chemical expansion is dominated by the GDC layer exposed to the fuel electrode.

We also point out that this study is limited to the calculation of elastic stresses, assuming homogeneous materials. Crack nucleation and propagation are not considered. It is conceivable that residual porosity in the electrolyte plays a considerable role in stress concentration, and therefore the failure probability of the electrolyte layers will be difficult to predict from bulk mechanical data. Finally, while the failure of the electrolyte is clear from the experimental findings, it remains a hypothesis that the cracking initiates in the YSZ layer. This would need to be verified.

6. Summary and Conclusion

The present study shows that high-performance SOCs using a ceria-based, three-layer electrolyte suffer catastrophic damage at high current densities in SOEC operation. Using an adapted model to calculate the electro-chemo-mechanical stresses in the multilayer system as a function of the local chemical potential of oxygen, it is possible to show the dependence of the tensile stresses occurring in the electrolyte layer on the operation conditions in SOEC and SOFC mode. While the accuracy of the calculated stresses should be taken with caution due to the many assumptions and simplifications, the calculations clearly show how tensile stress increases near the air side of the electrolyte layer with increasing current density in SOEC operation. They also show that SOFC operation should be uncritical with such a supported cell, even at a temperature of 800 °C despite the GDC electrolyte. A key finding of this study is the opposing influence of

temperature on the reducibility of ceria and the fuel electrode polarization, resulting in a non-monotonous temperature dependence of the maximum tensile stress. The detailed understanding provided by this study opens up the possibility to engineer such cells towards improved stability with an understanding of all the relevant parameters.

Acknowledgements

The authors would like to appreciate Frank Vondahlen and Dr. Sven Uhlenbruck (IEK-1 in Forschungszentrum Jülich, Germany) for their help with the physical vapor deposition, Dr. Doris Sebold for her help with the SEM investigations, and the partial financial support from China Scholarship Council (CSC No. 201606460053).

References

[1] Sunfire, Successful test operation of the world's largest high-temperature electrolysis module, https://www.sunfire.de/en/news/detail/successful-test-operation-of-the-worlds-largest-high-temperature-electrolysis-module (2021).
[2] R. Peters, M. Frank, W. Tiedemann, I. Hoven, R. Deja, N. Kruse, Q. Fang, L. Blum, R. Peters, Journal of the Electrochemical Society, 168 (2021) 014508.
[3] C. Bischof, A. Nenning, A. Malleier, L. Martetschläger, A. Gladbach, W. Schafbauer, A.K. Opitz, M. Bram, International Journal of Hydrogen Energy, 44 (2019) 31475-31487.
[4] C. Lenser, H. Jeong, Y.J. Sohn, N. Russner, O. Guillon, N.H. Menzler, Journal of the American Ceramic Society, 101 (2017) 739-748.
[5] S.R. Bishop, K.L. Duncan, E.D. Wachsman, Electrochimica Acta, 54 (2009) 1436-1443.
[6] A. Atkinson, Solid State Ionics, 95 (1997) 249-258.
[7] S. Zhu, Y. Wang, Y. Rao, Z. Zhan, C. Xia, International Journal of Hydrogen Energy, 39 (2014) 12440-12447.
[8] Z.-H. Jin, Journal of Applied Physics, 102 (2007) 083533.
[9] Y.-D. Kim, J. Yang, J.-I. Lee, M. Saqib, J.-S. Shin, K. Park, M. Jo, S.-J. Song, J.-Y. Park, Journal of Power Sources, 452 (2020) 227758.

[10] M. Mogensen, N.M. Sammes, G.A. Tompsett, Solid State Ionics, 129 (2000) 63-94.
[11] S. Wang, T. Kobayashi, M. Dokiya, T. Hashimoto, Journal of The Electrochemical Society, 147 (2000) 3606-3609.
[12] S.R. Bishop, K.L. Duncan, E.D. Wachsman, Acta Materialia, 57 (2009) 3596-3605.
[13] A. Atkinson, T.M.G.M. Ramos, Solid State Ionics, 129 (2000) 259-269.
[14] T. Jacobsen, M. Mogensen, ECS Transactions, 13 (2008) 259-273.
[15] I. Riess, Journal of The Electrochemical Society, 128 (1981) 2077-2081.
[16] M. Gödickemeier, L.J. Gauckler, Journal of The Electrochemical Society, 145 (1998) 414-421.
[17] S. Dierickx, T. Mundloch, A. Weber, E. Ivers-Tiffée, Journal of Power Sources, 415 (2019) 69-82.
[18] C.H. Hsueh, Thin Solid Films, 418 (2002) 182-188.
[19] F.L. Lowrie, R.D. Rawlings, Journal of the European Ceramic Society, 20 (2000) 751-760.
[20] J. Kondoh, H. Shiota, K. Kawachi, T. Nakatani, Journal of Alloys and Compounds, 365 (2004) 253-258.
[21] S. Giraud, J. Canel, Journal of the European Ceramic Society, 28 (2008) 77-83.
[22] M. Cheng, in, The University of Arizona., 2002.
[23] A. Ghazanfari, W. Li, M.C. Leu, J.L. Watts, G.E. Hilmas, Ceramics International, 43 (2017) 6082-6088.
[24] T. Kushi, K. Sato, A. Unemoto, S. Hashimoto, K. Amezawa, T. Kawada, Journal of Power Sources, 196 (2011) 7989-7993.
[25] Y. Wang, K. Duncan, E.D. Wachsman, F. Ebrahimi, Solid State Ionics, 178 (2007) 53-58.
[26] D.-W. Ni, B. Charlas, K. Kwok, T.T. Molla, P.V. Hendriksen, H.L. Frandsen, Journal of Power Sources, 311 (2016) 1-12.
[27] A. Nakajo, C. Stiller, G. Härkegård, O. Bolland, Journal of Power Sources, 158 (2006) 287-294.
[28] S. Watanabe, S. Sukino, T. Miyasaka, K. Sato, K. Yashiro, T. Kawada, T. Hashida, Journal of Materials Science, 55 (2020) 8679-8693.
[29] D. Klotz, A. Weber, E. Ivers-Tiffée, Electrochimica Acta, 227 (2017) 110-126.
[30] W. Schafbauer, N.H. Menzler, H.P. Buchkremer, International Journal of Applied Ceramic Technology, 11 (2014) 125-135.
[31] A. Weber, A. Müller, D. Herbstritt, E. Ivers-Tiffée, ECS Proceedings Volumes, 2001-16 (2001) 952-962.
[32] M. Kornely, A. Leonide, A. Weber, E. Ivers-Tiffée, Journal of Power Sources, 196 (2011) 7209-7216.
[33] A. Leonide, V. Sonn, A. Weber, E. Ivers-Tiffée, Journal of The Electrochemical Society, 155 (2008) B36-B41.
[34] A. Leonide, S. Hansmann, E. Ivers-Tiffée, ECS Transactions, 28 (2010) 341-346.
[35] J.C. Njodzefon, D. Klotz, A. Kromp, A. Weber, E. Ivers-Tiffée, Journal of The Electrochemical Society, 160 (2013) F313-F323.
[36] D. Udomsilp, C. Lenser, O. Guillon, N.H. Menzler, Energy Technology, 9 (2021) 2001062.
[37] A. Beez, X. Yin, N.H. Menzler, R. Spatschek, M. Bram, Journal of The Electrochemical Society, 164 (2017) F3028-F3034.
[38] C.E. Frey, Q. Fang, D. Sebold, L. Blum, N.H. Menzler, Journal of The Electrochemical Society, 165 (2018) F357-F364.
[39] B.-K. Park, Q. Zhang, P.W. Voorhees, S.A. Barnett, Energy & Environmental Science, (2019).
[40] L. Zhang, L. Zhu, A.V. Virkar, Journal of The Electrochemical Society, 166 (2019) F1275-F1283.